Nonlinear Processes
in Geophysics
Discussions

Open Access

EGU

1 **Spatial and radiometric characterization of multi-spectrum**

2 **satellite images through multifractal analysis**

3

4 **Carmelo Alonso[1,2], Ana M. Tarquis[2,3], Ignacio Zúñiga[4] and Rosa M. Benito[2]**

5

6 [1]Earth Observation Systems, Indra Sistemas S.A., Madrid, Spain.

7

8 [2]Grupo de Sistemas Complejos, U.P.M, Madrid, Spain.

9

10 [3]CEIGRAM, E.T.S.I.A.A.B., U.P.M, Madrid, Spain.

11

12 [4]Dpt. Física Fundamental, Facultad de Ciencias, Universidad Nacional de Educación a
13 Distancia (UNED), Madrid, Spain.

14

15

16

17 Corresponding author: Ana M. Tarquis (anamaria.tarquis@upm.es)

18
19

1

Nonlinear Processes
in Geophysics

Discussions

Open Access

EGU

1 **Spatial and radiometric characterization of multi-spectrum**

2 **satellite images through multifractal analysis**

3

4 **Abstract:** Several studies point out that vegetation indexes can been used to estimate root

5 zone soil moisture and earth surface images, obtained by high resolution satellites, give

6 presently huge information on these indexes based in several wavelengths data. Because of

7 the potential capacity for systematic observations at various scales, remote sensing technology

8 extends possible data archives from present time to over several decades back. For this

9 advantage, enormous efforts have been made by researchers and application specialists to

10 delineate vegetation indexes from local scale to global scale by applying remote sensing

11 imagery.

12 In this work, four bands images have been considered, involved in these vegetation indexes,

13 taken by satellites IKONOS-2 and LANDSAT-7 of the same geographic location to study the

14 effect of both spatial (pixel size) and radiometric (number of bits coding the image) resolution

15 on these wavelength bands.

16 In order to do so, a multifractal analysis of these multi-spectral images was applied in each of

17 these bands. The results showed that spatial resolution has a similar scaling effect in the four

18 bands, but radiometric resolution has a larger influence in Blue and Green bands than in Red

19 and Near InfraRed bands. This information should be taken in to account when vegetation

20 indexes based on different satellite sensors are obtained.

21

22

23 **Keywords:** vegetation index, wavelengths pattern, multifractal spectrum

24

Nonlinear Processes in Geophysics

Discussions

Open Access

EGU

1 Introduction

Soil moisture is a critical condition affecting interaction of land surface and atmosphere. Remotely sensed data is an important source of information and it can indirectly measure soil moisture in space and time. However, the signal only penetrates the top few centimeters, and soil moisture at deeper layers must be estimated. One method to estimate soil moisture at deeper layers is through vegetation indices. Several authors have investigating the potential of vegetation indices to estimate root zone soil moisture. The Normalized Difference Vegetation Index (NDVI) and Enhanced Vegetation Index (EVI) have been used by several authors (Wang et al., 2007; Ben-Ze'ev et al., 2006; Deng et al., 2007) in different conditions finding significant estimations with root zone soil moisture. For the estimation of these indexes NIR, Red and Blue wavelengths are needed (Huete et al., 2014).

The images provided by the satellites show the land surface in a wide range of wavelengths (from visible to thermal infrared or microwaves) and also with a great variety of spatial resolutions (from a few kilometres to tens of centimeters). The analysis of these varied images and their synergic possibilities are a challenging problem especially with new sensors, which have small spatial resolution and a large range of radiometric quantification. Fractal analysis offers significant potential for improvement in the measurement and analysis of spatially and radiometrically complex remote sensing data. This analysis also provides quantitative insight on the spatial complexity in the information of the landscape contained within these data.

In the general mathematical framework of fractal geometry many analytical methods have been developed; to name a few: textural homogeneity has been characterized using the fractal dimension (Fioravanti, 1994); it has also been used as a spatial measure for describing the complexity of remote sensing imagery (Lam and De Cola, 1993); changes in the image complexity have been detected through the spectral range of hyperspectral images affecting the fractal dimension (Qiu et al. 1999); similarly De Cola (1989) and Lam (1990) have found that fractal dimension also depends on the spectral bands of Landsat TM imagery.

1 Motivated by the fractal geometry of sets (Mandelbrot, 1983), the development of multifractal

2 theory, introduced in the context of turbulence, has been applied in many areas such as

3 earthquake distribution analysis (Hirata and Imoto, 1991), soil pore characterization

4 (Kravchenko et al. 1999; Tarquis et al. 2003), image analysis (Sánchez et al. 1992) or remote

5 sensing (Tessier et al., 1993; Cheng and Agterberg, 1996; Schmitt et al., 1997; Laferrière and

6 Gaonac'h, 1999; Cheng, 1999; Lovejoy et al., 2001b; Du and Yeo, 2002; Parrinello and

7 Vaughan, 2002; Harvey et al., 2002; Turiel et al. 2005).

8

9 The acquisition of remotely sensed multiple spectral images is thus a unique source of data

10 for determining the scale invariant characteristics of the radiance fields related to many

11 factors, such as soil and bedrock chemical composition, humidity content and surface

12 temperature (e.g., Laferrière and Gaonac'h, 1999; Maìtre and Pinciroli, 1999; Lovejoy et al.,

13 2001a, b; Harvey et al., 2002; Beaulieu and Gaonac'h, 2002; Gaonac'h et al., 2003; Cheng,

14 2004). In the multifractal scheme used, the satellite image is considered as a singular measure

15 and it is analyzed through a multifractal (MF) spectrum, which gives either geometrical or

16 probabilistic information about the pixels distribution with the same singularity.

17

18 The aim of this work is to characterize by MF analysis the image patterns in the wavelength

19 ranges used for NDVI, EVI and Green bands. In order to investigate how the image

20 information is affected by the sampling with different spatial and radiometric resolutions, we

21 have also analyzed images of the same site but acquired by two different satellites: Landsat-7

22 and Ikonos-2.

23

24 We present a comparative analysis of multifractal (MF) tools applied to multi-spectral images

25 obtained by IKONOS-2 and LANDSAT-7. Both satellites have several bands in visible and

26 near-infrared spectral regions in common that can be used in vegetation indexes estimation.

27 However the bands have different spatial resolution, 4 m for IKONOS and 30 m for

28 LANDSAT-7, and radiometric resolution, 11 and 8 bits respectively. The bands we have

29 chosen are Red (R), Green (G), Blue (B) and Near InfraRed (NIR). For each of those bands,

30 the MF spectrum has been calculated directly from the Hölder exponents α and the

31 singularities spectrum f(α).

Nonlinear Processes
in Geophysics

Open Access

Discussions

EGU

1   **2   Materials and methods**

2   **2.1   Images**

3   As already noted, in this work we have analysed two images of the same site acquired from

4   different satellites, Landsat-7 and Ikonos-2. Both are multi-spectral images with several bands

5   that cover several regions of the electromagnetic spectrum in the visible and near infrared

6   wavelength.

7

8   Landsat-7 was put in orbit in April 1999. This satellite follows a sun-synchronous orbit at 705

9   km of altitude, with an equatorial crossing time of 10:00 a.m. in the descending node. It

10   requires 98.8 min to circle the Earth, tracing a worldwide reference system (WRS) of just

11   over 230 ground paths. During at least three decades Landsat orbits over each of these paths

12   once every 16 days in a repetitive cycle (Mika, 1997).

13

14   The main Landsat-7 sensor for Earth observation is the Enhanced Thematic Mapper Plus

15   (ETM+). The ETM+ operates as a whiskbroom scanner and acquires data for seven spectral

16   bands: visible (ETM+#1, from 0.45 to 0.52 μm; ETM+#2, from 0.53 to 0.61 μm; ETM+#3,

17   from 0.63 to 0.69 μm), near infrared (ETM+#4, from 0.78 to 0.9 μm), shortwave infrared

18   (ETM+#5, from 1.55 to 1.75 μm, and ETM+#7, from 2.09 to 2.35 μm) and thermal infrared

19   (ETM+#6, from 10.4 to 12.5 μm). The ETM+ ground sampling distance (pixel size in the

20   images) is 30 m for the six reflective bands and 60 m for the thermal band. The ETM+ also

21   acquires images for a panchromatic band (ETM+#8, from 0.52 to 0.9 μm) with a 15 m ground

22   sampling distance. The radiometric resolution of the Landsat-7 data is 8 bit/pixel or 256 grey

23   levels for the pixel digital value.

24

25   Ikonos-2 was launched in September 1999. Its panchromatic sensor, with a resolution of 0.82

26   m, provided the first very high resolution images of the Earth's surface from EOS. The Ikonos

27   orbit altitude is approximately 681 km, it is inclined 98.1 degrees to the equator and it

28   provides sun-synchronous operation. The equatorial crossing time of Ikonos is 10:30 a.m. in

5

Nonlinear Processes
in Geophysics
Discussions

1   the descending node. The orbit provides daily access to sites within 45 degrees of nadir (Dial

2   et al. 2003).

3

4   The multi-spectral sensor simultaneously collects blue (IK#1, from 0.445 to 0.516 μm), green

5   (IK#2, from 0.506 to 0.595 μm), red (IK#3, from 0.632 to 0.698 μm) and near infrared (IK#4,

6   from 0.757 to 0.853 μm) bands with 3.28 meter resolution at nadir. Both images,

7   panchromatic and multi-spectral, have a radiometric resolution of 11 bits/pixel or 2048 grey

8   levels for the pixel digital value.

9

10   The Landsat-7 multi-spectral image used in this study was acquired on August 6th 2000 at

11   10:46 a.m. and it corresponds to the scene with WRS coordinates, path and row: 201 - 32.

12   This scene is located in the central region of Spain and it covers a square surface of

13   approximately 180 km side-length, located around Madrid. Solar azimuth and elevation

14   angles for this scene are 132.44 and 58.62 degrees respectively.

15

16   The Ikonos data used in this study is a multi-spectral image acquired on August 8th 2000 at

17   11:03 a.m. It covers a square area of 11 km side located near Aranjuez, south of Madrid, in

18   the central region of Spain. Solar azimuth and elevation angles for this scene are 139.5 and

19   60.79 degrees respectively. Both images were corrected geometrically to the same

20   cartographic projection: UTM, zone 30 N by a co-registration process.

21

22   The analysis has been carried out on a subset that covers (approximately) the same area in

23   both the Landsat and the Ikonos images, corresponding to a region located north the town of

24   Aranjuez. The representative elements of the land used in the selected area are: irrigate crops,

25   pastures, heaths, unirrigated land cultivations and olive groves. The Landsat subset is a

26   rectangle of 772 x 824 pixels with a size of 30 m. The Ikonos image consists of a square

27   subset with 2046 x 2046 pixels and 4 m resolution.

28

Nonlinear Processes
in Geophysics
Discussions

Open Access

EGU

1   **2.2   Multifractal image analysis**

2   A multifractal analysis is basically the measurement of a statistic distribution and therefore

3   gives useful information even if the underlying structure does not show a full self similar

4   behaviour (Plotnick et al., 1996).

5

6   A monofractal object can be measured by counting the number N of δ size boxes needed to

7   cover the object. The measure depends on the box size as

8      $N(\delta) \propto \delta^{-D_0}$ (1)

9   where

10     $D_0 = \lim_{\delta \to 0} \dfrac{\log N(\delta)}{\log \dfrac{1}{\delta}}$ (2)

11   is the fractal dimension. D_0 is calculated from slope of a log-log plot.

12

13   There are several methods for implementing multifractal analysis; in this section the choose

14   moment method (Halsey et al., 1986) is explained. This method uses mainly three functions:

15    $\tau(q)$, known as the mass exponent function, α, the coarse Hölder exponent, and $f(\alpha)$,

16   multifractal spectrum. A measure (or field), defined in two-dimensional image embedding

17   space ($n \times n$ pixels) and with values based on grey tones (for 8 bit goes from 0 to 255),

18   cannot be consider as a geometrical set and therefore cannot be characterized by a single

19   fractal dimension.

20

21   Applying disjoint covering by boxes in an "up-scaling" partitioning process we obtain the

22   partition function $\chi(q,\delta)$ (Feder, 1989) defined as:

23     $\chi(q,\delta) = \sum_{i=1}^{N(\delta)} \mu_i^q(\delta) = \sum_{i=1}^{N(\delta)} m_i^q$ (3)

24

Nonlinear Processes
in Geophysics

Open Access

Discussions

EGU

1   where m is the mass of the measure, q is the mass exponent, δ is the length size of the box

2   and $N(\delta)$ is the number of boxes in which $m_i > 0$. Based on this, the mass exponent function

3   $\tau(q)$ shows how the moments of the measure scales with the box size:

4   $$\tau(q) = \lim_{\delta \to 0} \frac{\log < \chi(q,\delta) >}{\log(\delta)} = \lim_{\delta \to 0} \frac{\log < \sum_{i=1}^{N(\delta)} m_i^q >}{\log(\delta)}$$ (4)

5   where $<>$ represents statistical moment of the measure $\mu_i(\delta)$ defined on a group of non

6   overlapping boxes of the same size partitioning the area studied.

7

8   The singularity index, α, can be determined by the Legendre transformation of the $\tau(q)$ curve

9   (Halsey, 1986) as:

10   $$\alpha(q) = \frac{d\tau(q)}{dq}$$ (5)

11

12   The number of cells of size δ with the same α, $N_\alpha(\delta)$, is related to the cell size as

13   $N_\alpha(\delta) \propto \delta^{-f(\alpha)}$, where $f(\alpha)$ is a scaling exponent of the cells with common α. Parameter

14   $f(\alpha)$ can be calculated as:

15   $$f(\alpha) = q\alpha(q) - \tau(q)$$ (6)

16

17   Multifractal spectrum (MFS) shown as plot of α vs. $f(\alpha)$, quantitatively characterizes

18   variability of the measure studied with asymmetry to the right and left indicating domination

19   of small and large values respectively (Evertsz and Mandelbrot, 1992). The width of the MF

20   spectrum (Δ) indicates overall variability (Tarquis et al., 2001; 2014).

21

1 ## 3   Results and Discussion

2 ### 3.1   Radiometric influence in the Multifractal spectrum

3 We first discuss the results obtained for the 2046 x 2046 pixels Ikonos image shown in Fig. 1,

4 in bands combination of false colour (IK#4, IK#3, IK#2 bands combination in RGB

5 visualization). In Fig. 2 IK#1, IK#2, IK#3, IK#4 bands histograms are shown. In the left

6 column are histograms with the original radiometric resolution and in the left column the

7 corresponding histograms rescaled to 8 bits. The histograms present a bimodal structure with

8 a narrow peak of low value pixels (dark grey) showing a sharp maximum and a wider peak

9 around a second lower maximum. For bands IK#1, IK#2, IK#3 the narrow peak maximum

10 corresponds to vegetation, mainly irrigate crops, showing strong water absorption. This effect

11 is particularly important in band IK#3. High value pixels (lighter grey) correspond to ground

12 zones with lower vegetation content. However, as vegetation shows high reflectivity in the

13 near infrared, IK#4 band histogram shows a predominance of high values pixels (lighter grey

14 pixels) corresponding to dense vegetation parts.

15

16 We cover the image with boxes of size $\delta = 2^{-n}$ and we change the box size from 2048 to 2

17 pixels, that is, $\delta = 2048 / 2^n$ with $n = 0, 1, 2,..., 10$. For each value of the parameter q, from -5

18 to +5 with increments of 0.5, the partition function (equation 3) is computed and $\chi(q, \delta)$ vs

19 $\log \delta$ is plotted in Fig. 3. Each graph contains 11 points. Linear fits of these points with least-

20 square provides the values of $\tau(q)$ and using Eq. [5-6] $\alpha(q)$ and $f(\alpha)$ are obtained. The MF

21 spectra $f(\alpha)$ corresponding to the four bands of multispectral Ikonos images are shown in

22 Fig. 4. Some characteristic parameters obtained from these MF spectra are shown in Table 1.

23 For each band $\alpha(q)$ values for $q = \{0, 1, 2\}$ are show. The first value corresponds to the

24 maximum of MFS and it is related to the box-counting dimension where the measure is

25 defined; the second value is related to information dimension and the third with the

26 correlation dimension. We split the MF spectra in two sections. Section I correspond to values

27 $\alpha(q) < \alpha(0)$ or $q > 0$ and section II to values with $\alpha(q) > \alpha(0)$ or $q < 0$. In section I the

28 amplitude, or semi-width, was calculated with differences $\Delta^+ = \alpha(0) - \alpha(+5)$, and in section II

29 with $\Delta^- = \alpha(-5) - \alpha(0)$. These two values for Ikonos bands are shown in the two last

Nonlinear Processes
in Geophysics
Discussions

Open Access

EGU

1   columns in Table 1. Note that amplitud Δ^+ decreases as bands wavelength grows whereas the

2   other amplitude Δ^- diminishes.

3

4   To study the influence of radiometric resolution on Ikonos image information complexity, the

5   original pixel code (11 bits) has been transform to 8 bits through a rescaling based on

6   minimum and maximum values between 0 and 255, preserving the initial histogram shape. In

7   figure 2 both the original histograms (left column) and the rescale histograms (right column)

8   are shown.

9

10 The MF spectrum obtained after this transformation is shown in figure 4 (upper part) and the

11 corresponding new parameters in Table 2. In this case both Δ^+ and Δ^- increase as the

12 wavelength increases for the three visible bands, but decreasing for the near infrared band.

13

14 **3.2   Spatial resolution influence in the Multifractal spectrum**

15 In order to avoid any other effect beside the spatial resolution a comparison between Landsat

16 (with an original pixel code of 8 bits) and the rescaled histograms from Ikonos is made. In this

17 section we discuss the results obtained in the MF analysis on 772 x 828 pixels Landsat image

18 shown in Figure 5, in bands combination of false colour (ETM+#4, ETM+#3 and ETM+#2

19 bands combination in RGB visualization). The yellow rectangle corresponds to the area

20 covered for the Ikonos image. Frequency values histograms of these bands are showed in the

21 right column of Figure 5.

22

23 In the calculations, box sizes range from 512 to 2 pixel, that is, $\delta = 512/2^n$ with $n = 0, 1,...8$.

24 For each value of the parameters q, from -5 to +5 with increments of 0.5, we compute the

25 partition function, and $\chi(q,\delta)$ vs $\log\delta$ are plotted in Figure 6. In this case each linear fits

26 contains only 9 points. The MF spectra, $f(\alpha)$, corresponding to the first four bands of

27 multispectral Landsat images are shown in Figure 7.

28

1   From a comparison of figures 4 and 7 we see that Landsat images MF spectra are always

2   located inside the corresponding Ikonos MF spectra. For a given value of Hölder exponent α

3   the relation $f_{Landsat}(\alpha) \leq f_{Ikonos}(\alpha)$ is always satisfied. This result means that Landsat images

4   show lower complexity than Ikonos images. As stated in section 3.1 Ikonos satellite data are

5   coded in 11 bits in contrast with Landsat 8 bits coded data. Higher radiometric resolution

6   gives a higher range of possible grey values per pixel. Note that this radiometric resolution

7   effect is manifested in both sections of the MF spectra (I, $q > 0$, and II, $q < 0$).

8

9   The MF spectra parameters are shown in Table 3. In general, Landsat bands present a low

10   degree of multifractality similar to Ikonos images coded at 8 bits. This is also true among the

11   different bands, presenting low variations among them in a range of 1.3 and 1.4. Landsat

12   bands do not show a clear relationship between multifractality and wave length, being the

13   near infrared the lowest multifractality value.

14

15   **4   Conclusions**

16   In this work, we have used MF spectra as a successful technique for analyzing common

17   information contained in multi-spectral images of the site of the Earth surface acquired by two

18   satellites, Landsat-7 and Ikonos, in four common bands in the visible (blue, green and red)

19   and near-infrared wavelength regions used in several vegetation indexes.

20

21   The radiometric resolution has been studied comparing MF spectra of the images acquired by

22   Ikonos-2 coded in 11 bits and transformed in 8 bits code. The results obtained after the

23   histogram transformation in the blue and green bands were the ones you would expected after

24   the simplification applied from 11 to 8 bits, i.e. higher frequency in all the histogram bin

25   values (see figure 2). In contrast, red and infrared bands showed no sensitivity at all to this

26   transformation keeping the same MF spectra. To our knowledge, this is the first time these

27   differences among bands are reported.

28

1 In order to analyse the effect of spatial resolution in each band at 4 m (Ikonos with 8 bits)

2 pixel size and 30 m (Landsat with 8 bits) pixel size are compared. Obviously, the higher the

3 spatial resolution, the higher the Hölder spectrum amplitude in the green and blue bands are.

4 In fact, observing the graphics of the three cases studied (Ikonos 11 bits, Ikonos 8 bits and

5 Landsat 8 bits) both bands gradually reduce their $\alpha(q)$ amplitude in the negative as well as in

6 the positive q values. However, this is not the case for red and infrared bands that present a

7 huge difference between Ikonos and Landsat curves of the MF spectra. This implies that the

8 estimation in the vegetation indices from both sensors will be different.

9

10 In the $q > 0$ region for blue and green bands the sensitivity to both factors are very similar,

11 being the blue band ratio slightly higher. In the other two bands, red and infrared, for the same

12 region only present sensitivity to spatial resolution, showing a similar rate than blue and green

13 bands. Observing the $q < 0$ region for blue and green the behaviour is similar to the positive

14 one but with a lower ratio (between 1 and 2) and once more, the red and infrared bands don't

15 show any sensitivity to radiometric resolution. Nevertheless in the spatial resolution the red

16 band has a ratio similar to blue and green, and infrared shows the highest ratio (around 8)

17 pointing the extreme influence of the lowest values contained, see histograms in figure 2

18 (Ikonos-2 8 and 11 bits) and figure 5 (Landsat-7).

19

20 **Acknowledgements**

25

26

Nonlinear Processes
in Geophysics
Discussions

Open Access

EGU

1   References

2   Beaulieu, A. and Gaonac'h, H.: Scaling of differentially eroded surfaces in the drainage

3   network of the Ethiopian plateau, Rem. Sens. Environ., 82, 111–122, 2002.

4   Ben-Ze'ev, E., Karnieli, A., Agam, N., Kaufman, Y., Holben, B., Assessing Vegetation

5   Condition In The Presence Of Biomass Burning Smoke By Applying The Aerosol-Free

6   Vegetation Index (AFRI) On MODIS Images, International journal of remote sensing, 27,

7   3203-3221, 2006.

8   Cheng, Q. and Agterberg, F.P.: Multifractal modelling and spatial statistics. Mathematical

9   Geology, 28(1), 1-16, 1996.

10   Cheng, Q.: A new model for quantifying anisotropic scale invariance and for decomposition

11   of mixing patterns, Mathematical Geology, 36, 345–360, 2004.

12   De Cola, L., Fractal analysis of a classified Landsat scene. Photogrammetric Engineering and

13   Remote Sensing **55**(5). 1989.

14   Deng, FP, Su, GL, Liu, C, Seasonal Variation Of MODIS Vegetation Indexes And Their

15   Statistical Relationship With Climate Over The Subtropic Evergreen Forest In Zhejiang,

16   China, IEEE GEOSCIENCE AND REMOTE SENSING LETTERS, 4, 236-240, 2007.

17   Dial, G., Bowen, H., Gerlach, F., Grodecki, J. and Oleszczuk, R., IKONOS satellite, imagery

18   and products. *Remote Sensing of Environment* **88**, 23-36. 2003.

19   Du, G. and T.S. Yeo. A novel multifractal estimation method and its application to remote

20   image segmentation. IEEE Transactions on Geoscience and Remote Sensing **40**(4), 980-982.

21   2002.

22   Evertsz, C.J.G., Mandelbrot, B.B.. In *Chaos and Fractals: New Frontiers of Science*, Peitgen,

23   H., Jurgens, H. and Saupe Springer-Verlag D., Eds., New York, 921. 1992.

24   Feder, J. Fractals. Plenum Press, New York, 283pp., 1988.

25   Fioravanti, S., *Multifractals: theory and application to image texture recognition.* In "Fractals

26   in Geosciences and Remote Sensing", Proceedings of a joint JRC/EARSeL Expert meeting.

27   Ispra. Italy, 14 – 15 April 1994.

28   Gaonac'h, H., Lovejoy, S., and Schertzer, D.: Resolution dependence of infrared imagery of

29   active thermal features at Kilauea volcano. Int. J. Rem.Sens., 24, 2323-2324, 2003.

1   Halsey, T.C., Jensen, M.H., Kadanoff, L.P., Procaccia, I. and Shraiman, B.I.. Fractal measures

2   and their singularities: the characterization of strange sets. *Phys. Rev. A* **33**, 1141-1151. 1986.

3   Harvey, D.C., Gaonac'h, H., Lovejoy, S. and Sxhertzer, D. : Multrifractal characterization of

4   remotely sensed volcanic features: a case study from Kilauea volcano, Hawaii, Fractals, 10,

5   265-274, 2002.

6   Hirata, T. and Imoto, M., *Multifractal analysis of spatial distribution of micro-earthquakes in*

7   *the Kanto region*, Geophys. J. Int. **107**. 1991.

8   Huete, A., Miura, T., Yoshioka, H., Ratana, P. and Broich, M., *Indices of Vegetation Activity*

9   in "Biophysical Applications of Satellite Remote Sensing". Jonathan M. Hanes Editor,

10   Springer, 2014.

11   Kravchenko, A.N., Boast, C.W. and Bullock, D.G., *Multifractal analysis of soil spatial*

12   *variability*, *Agron. J.* **91**. 1999.

13   Laferrière, A. and Gaonac'h, H.: Multifractal properties of visible reflectance fields from

14   basaltic volcanoes, J.Geophys.Res., 104(B3), 5115-5126, 1999.

15   Lam, N.S. and De Cola, L., *Fractals in Geography*, Prentice Hall, Englewood Cliffs, New

16   Jersey. 1993.

17   Lam, N.S., *Description and measurement of Landsat TM images using fractals*.

18   Photogrammetric Engineering and Remote Sensing **56**(2), 1990.

19   Lovejoy, S., Pecknold, S., and Schertzer, D.: Stratified multifractal magnetization and surface

20   geomagnetic fields-I. Spectral analysis and modelling, Geophys. J. Int., 145, 112–126, 2001a.

21   Lovejoy, S., Schertzer, D, Tessier, Y. and Gaonach, H.: Multifractals and resolution-

22   independent remote sensing algorithms: the example of ocean colour. Int. J. Remote Sensing,

23   22(7), 119-1234, 2001b.

24   Maître, H. and Pinciroli, M.: Fractal characterization of a hydrological basin using SAR

25   satellite images, IEEE Trans. Geosci. Rem. Sens., 37, 175–181, 1999.

26   Mandelbrot, B. B. The Fractal Geometry of Nature, Freeman, San Francisco. 1983.

27   Mika, A.M., Three decades of Landsat instruments. Photogrammetric Engineering and

28   Remote Sensing **63**, 839-852. 1997.

Nonlinear Processes
in Geophysics
Discussions

Open Access

EGU

1 Parrinello, T. and R.A. Vaughan. Multifractal Analysis and feature extraction in satellite

2 imagery. Int. J. of Remote Sensing **23**(9), 1799-1825. 2002.

3 Plotnick R.E., Gardner, R.H., Hargrove, W.W., Prestegaard, K., Perlmutter, M.. Lacunarity

4 analysis: a general technique for the analysis of spatial patterns. Phys. Rev. E. 53(5), 5461-

5 5468. 1996.

6 Qiu, H., Lam, N.S., Quattrochi, D.A. and Gamon, J.A., *Fractal characterization of*

7 *hyperspectral imagery*, Photogrammetric Engineering and Remote Sensing **65**(1). 1999.

8 Sánchez, A., Serna, R., Catalina, F. and Afonso, C.N., *Multifractal patterns formed by laser*

9 *irradiation in GeAl thin multilayer films*, Physical Review B, **46**(1). 1992.

10 Schmitt, F., Schertzer, D., Lovejoy, S., and Marchal, P.: Multifractal analysis of satellite

11 images: towards an automatic segmentation. In *Fractals in Engineering* (Arcachon: Jules),

12 103-109, 1997.

13 Tarquis, A.M., Platonov, A., Matulka, A., Grau, J., Sekula, E., Diez, M. and Redondo J. M.

14 Application of multifractal analysis to the study of SAR features and oil spills on the ocean

15 surface. Nonlin. Processes Geophys., 21, 439-450, 2014.

16 Tarquis, A.M., Giménez, D., Saa, A., Díaz, M.C. and Gascó, J.M., *Scaling and multiscaling*

17 *of soil pore systems determined by image analysis*, in "Scaling methods in soil physics". Ed.

18 Y. Pachepsky, D.E. Radcliffe and H. Magdi Selim. CRC Press. 2003.

19 Tarquis, A.M., Losada, J.C., Benito, R. and Borondo, F., Multifractal analysis of the Tori

20 destruction in a molecular Hamiltonian System. Phys. Rev. E. **65**, 0126213(9). 2001.

21 Tessier, Y., Lovejoy, S., Schertzer, D., Lavalle'e, D., and Kerman, B.: Universal multifractal

22 indices for the ocean surface at far red wavelengths. Geophysical Research Letters, 20, 1167-

23 1170, 1993.

24 Turiel, A., Isern-Fontanet, J., García-Ladona, E. and Font, J., Multifractal Method for the

25 Instantaneous Evaluation of the Stream Function in Geophysics Flows. Phys. Rev. Lett. **95**,

26 104502. 2005.

27 Wang, X., Xie, H., Guan, H., and Xiaobing, Z, Different responses of MODIS-derived NDVI

28 to root-zone soil moisture in semi-arid and humid regions, Journal of Hydrology, 340, 12– 24,

29 2007.

Nonlinear Processes
in Geophysics

Open Access

Discussions

EGU

1   Table 1. Parameters obtained from the multifractal spectrum from each band of Ikonos-2

2   image with a pixel size of 4 m and a radiometric resolution of 11 bits. . The amplitudes of α

3   values are presented as Δ^{+} and Δ^{-} corresponding to $\alpha(0)$- $\alpha(5)$ and $\alpha(-5)$- $\alpha(0)$ respectively.

4

	Band	q	$\alpha(q)$	Δ^{+}	Δ^{-}
IKONOS (11bits)	**IK#1**	0	2.096	0.418	0.256
		1	1.938		
		2	1.865		
	IK#2	0	2.111	0.377	0.313
		1	1.936		
		2	1.871		
	IK#3	0	2.120	0.348	0.382
		1	1.937		
		2	1.878		
	IK#4	0	2.067	0.290	0.470
		1	1.959		
		2	1.908		

5

6

7

8

Nonlinear Processes
in Geophysics

Discussions

Open Access

EGU
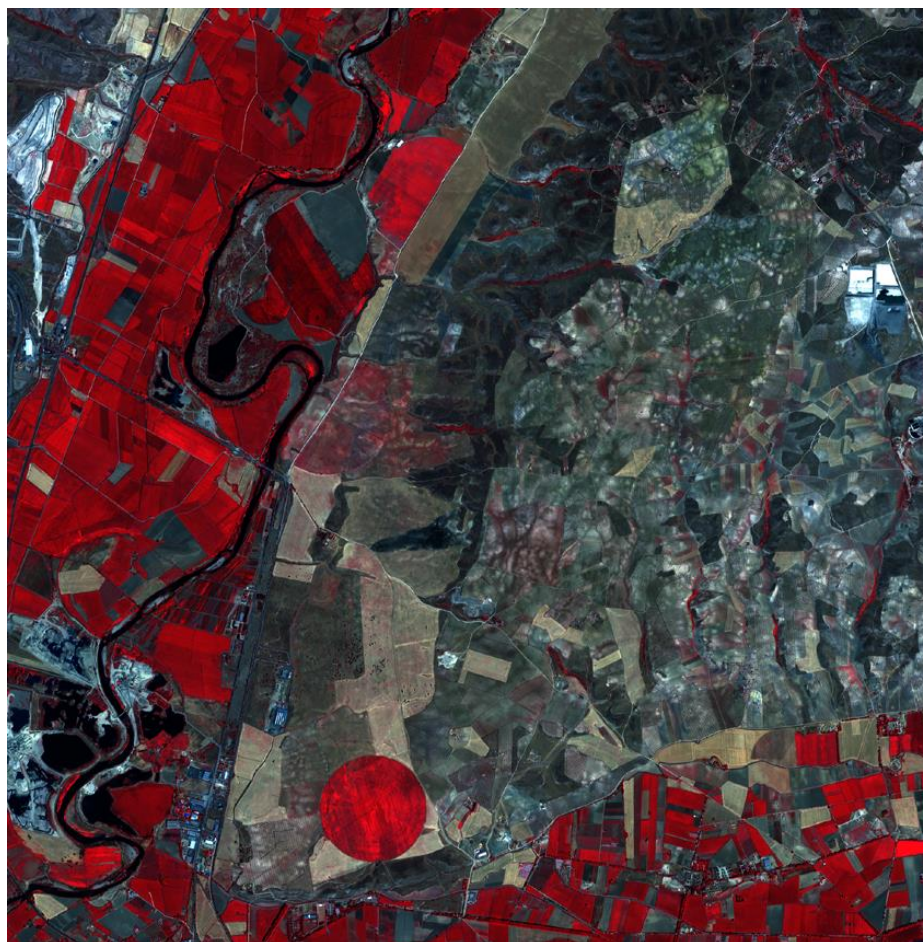
1   Table 2. Parameters obtained from the multifractal spectrum from each band of Ikonos-2

2   image with a pixel size of 4 m and a radiometric resolution of 8 bits. The amplitudes of α

3   values are presented as Δ^+ and Δ^- corresponding to $\alpha(0)- \alpha(5)$ and $\alpha(-5)- \alpha(0)$ respectively.

4

	Band	q	$\alpha(q)$	Δ^+	Δ^-
IKONOS **(8bits)**	**IK#1**	0	2.044	0.231	0.192
		1	1.971		
		2	1.930		
	IK#2	0	2.060	0.270	0.287
		1	1.963		
		2	1.914		
	IK#3	0	2.102	0.323	0.614
		1	1.945		
		2	1.887		
	IK#4	0	2.056	0.248	0.512
		1	1.966		
		2	1.923		

5

6

7

Nonlinear Processes
in Geophysics
Discussions

Open Access

EGU

1   Table 3. Parameters obtained from the multifractal spectrum from each band of Landsat

2   image with a pixel size of 4 m and a radiometric resolution of 8 bits. The amplitudes of α

3   values are presented as Δ^+ and Δ^- corresponding to α(0)- α(5) and α(-5)- α(0) respectively.

4

	Band	q	α(q)	Δ^+	Δ^-
Landsat	**ETM+#1**	0	2.021		
		1	1.985	0.160	0.119
		2	1.960		
	ETM+#2	0	2.018		
		1	1.988	0.119	0.119
		2	1.970		
	ETM+#3	0	2.016		
		1	1.989	0.095	0.110
		2	1.974		
	ETM+#4	0	2.017		
		1	1.989	0.106	0.104
		2	1.973		

5

6

7

1

2

Figure 1. The Ikonos-2 image in band combinations of false colour (IK#4, IK#3 and IK#2 in RGB). The image has a size of 2046 x 2046 pixels, each area unit correspond to 4x4 m. The coordinates UTM (zone 30) of the upper left and low right pixel in the image are: ULX = 446037 m, ULY = 4441672 m, LRX = 454221 m and LRY = 4433492 m.
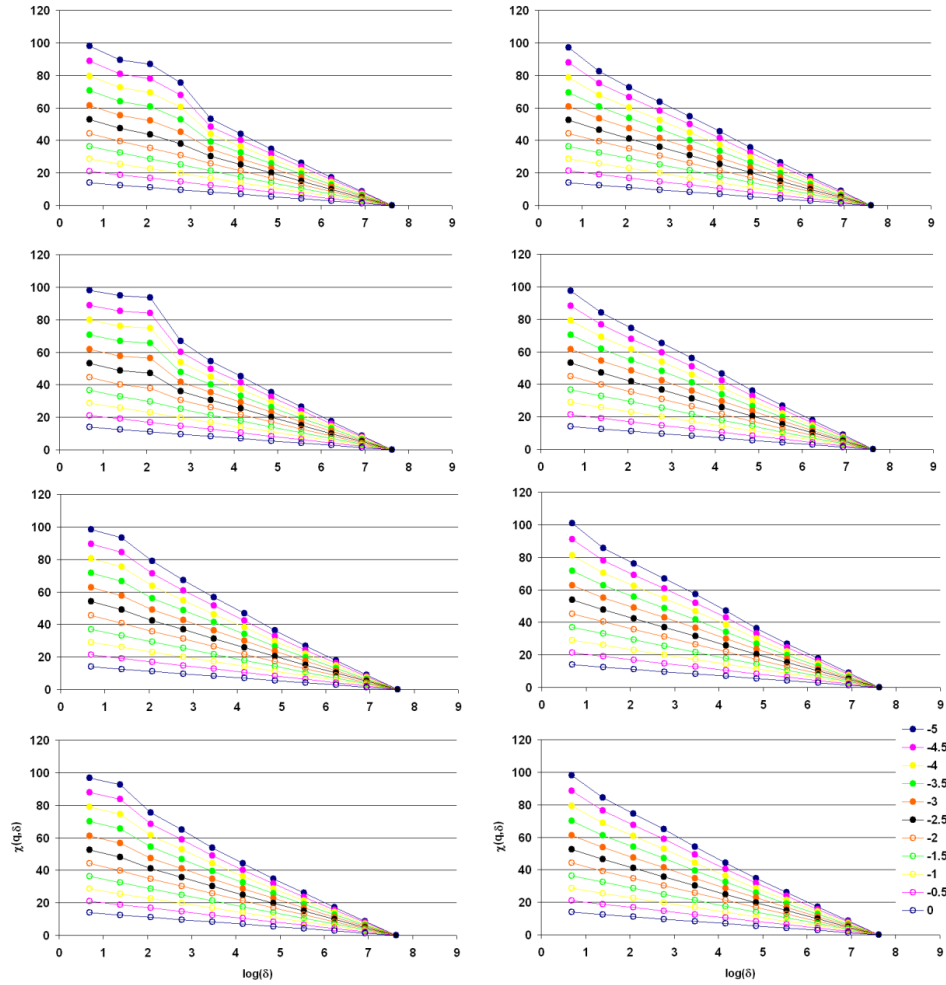
7

1
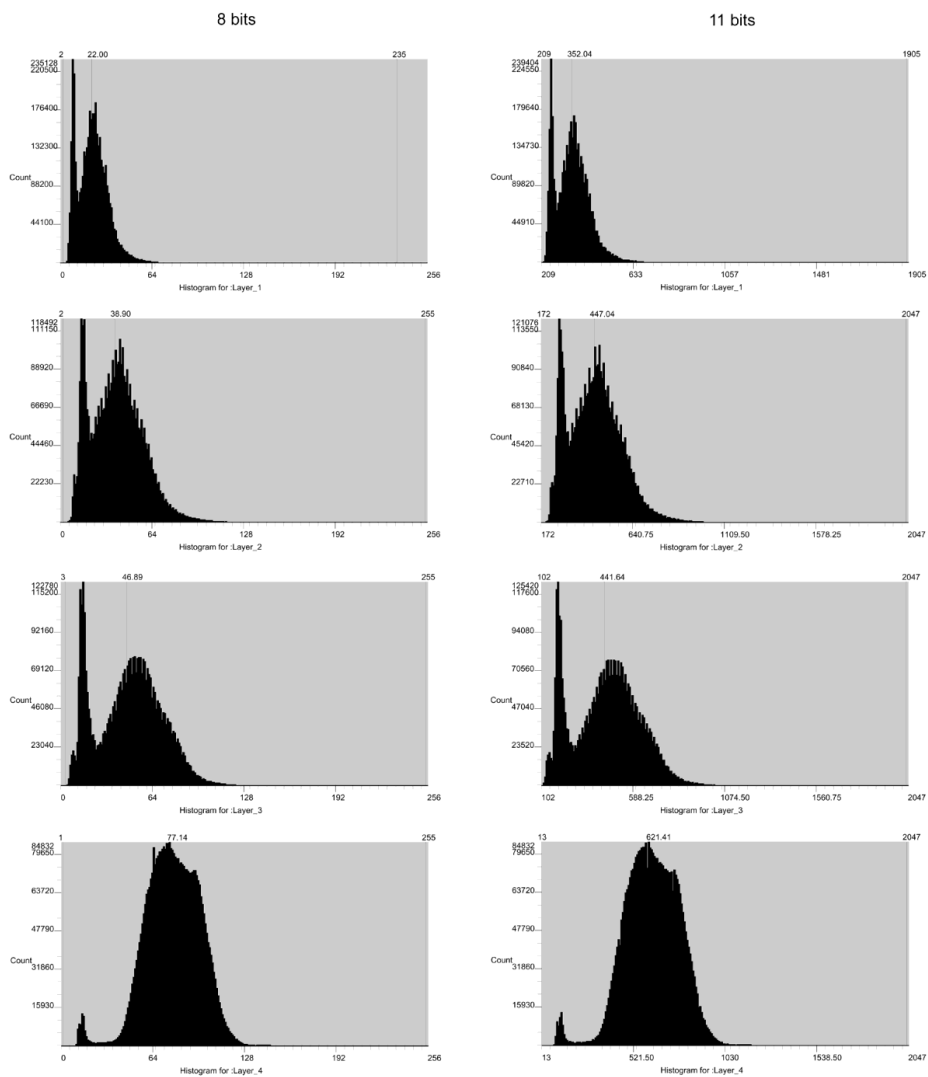
Figure 2. Histograms of the four bands of Ikonos-2 image for the original radiometric resolution, 11 bits (right), and the minimum-maximum rescale 8 bits radiometric resolution (left).

2

3

4

5

6

7

Figure 3. Plots of the partition function $\chi(q,\delta)$ versus $\log(\delta)$ for the first four bands of Ikonos-2 satellite and for $q < 0$ values. From top to bottom we show the results for IK#1, IK#2, IK#3 and IK#4. All the points are used for the fit and to calculate the slope for different values of q. The left column correspond to 8-bit image and the right column to 11 bit image.
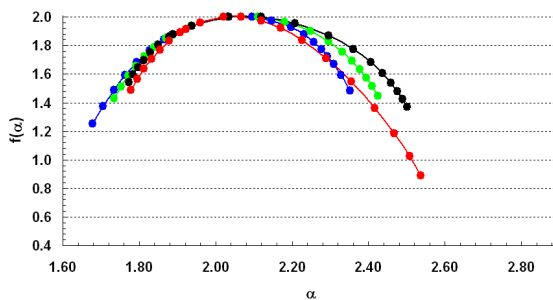
Nonlinear Processes
in Geophysics
Discussions

Open Access

EGU
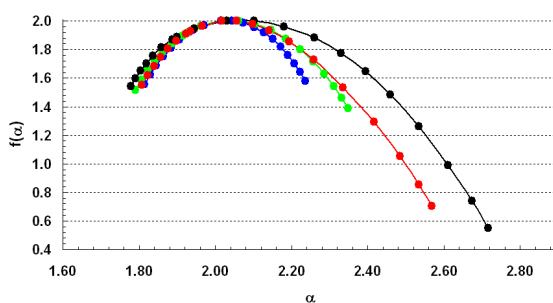
Figure 4. Multifractal spectrum of Ikonos-2 images for the original pixel values coded in 11 bits (lower) and the min-max rescale to 8 bits (upper), in each band analyzed: IK#1 in blue colour, IK#2 in green colour, IK#3 in red colour and IK#4 in black.

Nonlinear Processes
in Geophysics
Discussions

Open Access

EGU

1
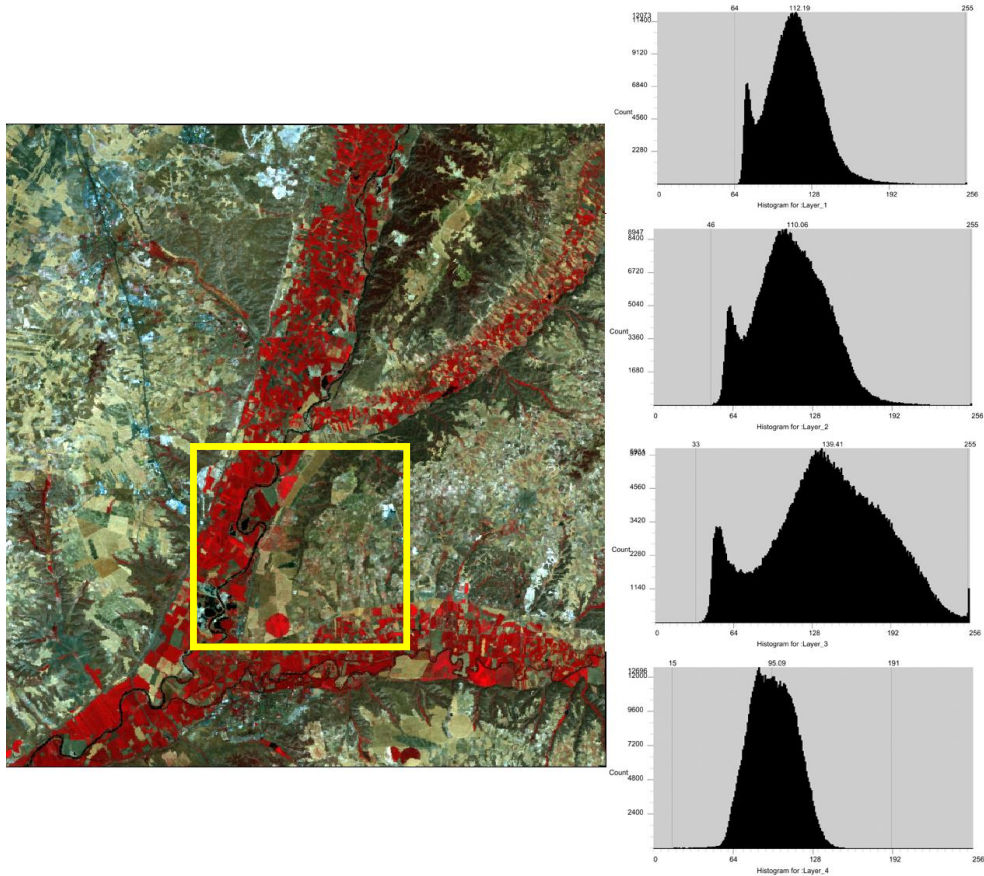
2   Figure 5. The Landsat-7 image and the histograms for the first four bands: blue (ETM+ #1),

3   green (ETM+ #2), red (ETM+ #3) and near infrared (ETM+ #4). The image has a size of

4   772x828 pixels, each area unit correspond to 30x30 m. The coordinates UTM (zone 30) of the

5   upper left and low right pixel in the image are: ULX = 438678 m, ULY = 4454134 m, LRX =

6   461808 m and LRY = 4429324 m.

7

8

9

10
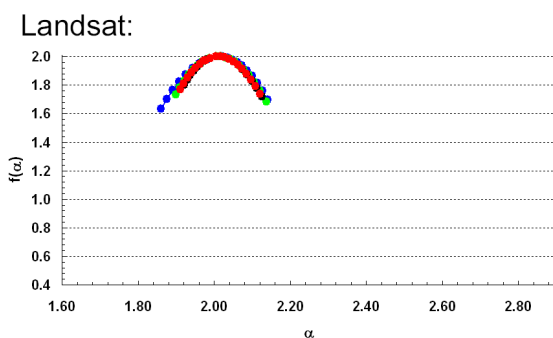
1
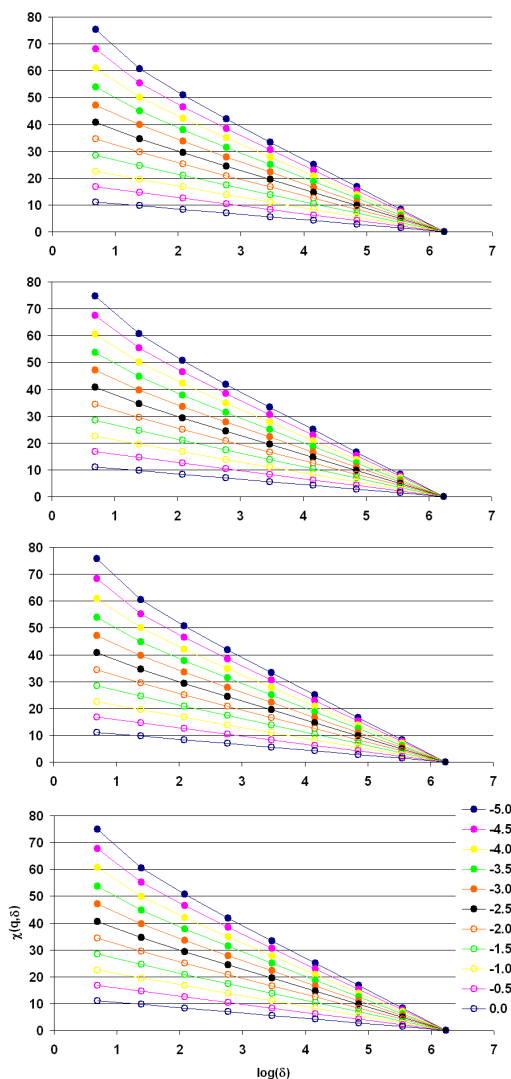
Figure 6. Plots of the partition function $\chi(q,\delta)$ versus $\log(\delta)$ for the first four bands of

Landsat satellite and for $q < 0$ values. From top to bottom we show the results for ETM+#1,

ETM+#2, ETM+#3 and ETM+#4. All the points are used for the regression line and to

calculate the slope for different values of q.

6

7

Nonlinear Processes
in Geophysics
Discussions

Open Access

EGU

1

2

3   Figure 7. Multifractal spectrum of Landsat images for the original pixel values coded in 8

4   bits, in each band analyzed: ETM+#1 in blue colour, ETM+#2 in green colour, ETM+#3 in

5   red colour and ETM+#4 in black.